Title
Vehicle Lateral Control under Fault in Front and/or Rear Sensors

Authors
Huang, Jihua
Lu, Guang
Tomizuka, Masayoshi

Publication Date
2000-12-01

This paper uses Postscript Type 3 fonts. Although reading it on the screen is difficult it will print out just fine.

CALIFORNIA PATH PROGRAM
INSTITUTE OF TRANSPORTATION STUDIES
UNIVERSITY OF CALIFORNIA, BERKELEY

Vehicle Lateral Control under Fault in Front and/or Rear Sensors

Jihua Huang, Guang Lu,
Masayoshi Tomizuka
University of California, Berkeley

California PATH Research Report
UCB-ITS-PRR-2000-25

This work was performed as part of the California PATH Program of the University of California, in cooperation with the State of California Business, Transportation, and Housing Agency, Department of Transportation; and the United States Department of Transportation, Federal Highway Administration.

Report for MOU 384

December 2000

ISSN 1055-1425

CALIFORNIA PARTNERS FOR ADVANCED TRANSIT AND HIGHWAYS

PROJECT TITLE:

Vehicle Lateral Control under Fault in Front and/or Rear Sensors

By

Jihua Huang

Guang Lu

Masayoshi Tomizuka

Department of Mechanical Engineering

University of California at Berkeley

Berkeley, CA 94720

Annual report for the first year of MOU 384

August 2000

Executive Summary

This report presents the research results of Memorandum of Understanding 384 (MOU384), *"Vehicle Lateral Control under Fault in Front and/or Rear Sensors"*, during 1999-2000. This project is a continuing effort of the Partners for Advanced Transit and Highways (PATH) on the research of passenger vehicles for Automated Highway Systems (AHS). The California PATH program was created to explore the possibilities of using advanced technologies to improve the efficiency and safety of highway transportation services in the state of california.

In an AHS, each vehicle is under computer control in both the longitudinal and the lateral directions. For vehicle lateral control, PATH has adopted the magnetic road reference system. Equally-spaced magnets are buried in the center of each automated lane. Magnetometers on board a vehicle sense the magnetic field generated by each magnet. The lateral controller calculates the lateral deviation from the outputs of the magnetometers and uses this information to set the steering command.

Earlier research efforts at PATH had concentrated on the lateral control of vehicles with the help of magnetometers installed under the front bumper of the vehicle alone. During the preparation for the National Automated Highway System Consortium (NAHSC) demonstration in 1997, it was realized that significantly better lane-keeping performance could be achieved by installing an additional set of magnetometers on the vehicle. This additional set of magnetometers was installed under the rear bumper of the vehicles.

Failure of components in the control system almost certainly leads to degraded operation and can potentially be a safety hazard. As part of an overall effort to build a reliable fault management system, MOU384 addresses the problem of developing degraded mode vehicle lateral control strategies. MOU384 is the first research project to systematically study vehicle lateral control strategies under faulty operation of the magnetometers. This project is primarily concerned with the following problems.

- lateral control of the vehicle using only one set of magnetometers
- autonomous lateral control based on Intelligent Ranging using Infrared Sensors (IRIS) (without the use of magnetometers)

Two output feedback controllers, the first using the output from the front set of magnetometers alone and the other using the output from the rear set of magnetometers alone, were designed based on the H_∞ optimal control technique. The controllers are optimal in the sense of minimizing the effects the disturbance (road curvature) and sensor noise on the lateral error and the control effort. Simulation results documenting the performance of these controllers are presented.

When both sets of magnetometers fail, the controlled vehicle has no direct measurements relative to the road. In this case, a possible backup scheme is to let the controlled vehicle follow its preceding vehicle. This vehicle following control algorithm is referred to as the Autonomous Lateral Control (ALC). An integrated lateral controller which uses IRIS along with the rear set of magnetometers is also developed. Simulation results for both ALC and the integrated vehicle lateral control scheme are presented in this report.

Abstract

This report documents the findings of research performed under MOU384, *"Vehicle Lateral Control under Fault in Front and/or Rear Sensors"* during the year 1999-2000. The objectives of the project are: (1) to study the behavior of existing vehicle lateral control systems in the event of magnetometer failures, (2) to design controllers that use the output from only one set of magnetometers, and (3) to develop an autonomous lateral control scheme that uses no magnetometers.

The performance of existing lateral control systems subject to magnetometer failures is evaluated based on both linearized and complex nonlinear vehicle models. Simulation results indicate that rear magnetometer failures result in degraded operation, and that front magnetometer failures cause instability in the control system.

Two output feedback controllers, one using the output of front magnetometers alone and the other using the output of rear magnetometers alone, are designed based on the H_∞ optimal control technique. The H_∞ optimal control procedure synthesizes optimal controllers which minimize the effects of disturbance and sensor noise on the lateral error and control effort. Simulations performed with these two controllers show satisfactory performance for longitudinal velocities up to $30m/s$.

When both front and rear magnetometers fail, autonomous lateral control based on Intelligent Ranging using Infrared Sensors (IRIS) allows the vehicle to follow its preceding vehicle. Simulation results for a platoon of three vehicles show that the lateral error of the leading vehicle is amplified by the following vehicles. An integrated controller that combines the information from IRIS and rear magnetometers is designed. Simulations show that this control scheme provides better tracking accuracy than autonomous lateral control.

Keywords: vehicle lateral control, bicycle model, H_∞ optimal control, autonomous lateral control, vehicle following.

1 Introduction

This project focuses on vehicle lateral control subject to magnetometer failures. The current PATH lateral control algorithms rely on the outputs of two sets of magnetometers, one installed under the front bumper of the vehicle and the other under the rear bumper of the vehicle. The first lateral controller developed by PATH utilized magnetometers at the front bumper only. It was recognized during the preparation for the 1997 National Automated Highway Systems Consortium (NAHSC) demonstration that installing a second set of magnetometers at the rear bumper helps to improve lane-keeping performance at high speeds. Since then, vehicle lateral control based only on front magnetometers at high speeds has not been fully studied. More significantly, vehicle lateral control based only on rear magnetometers has not been studied yet. Such studies are important because of safety concerns in the event of magnetometer failures.

MOU384 is the first research project to systematically study vehicle lateral control strategies under faulty operation of magnetometers. This project is a part of the fault management of vehicle lateral control in Automated Highway Systems. The main research topics concerned in this project are as follows.

- Evaluating the performance of the existing lateral control system of PATH under the scenario of magnetometer failures.
- Developing lateral controllers that use only one set of magnetometers (when the other set of magnetometers fails).
- Developing Autonomous Lateral Control (ALC) based on Intelligent Ranging using Infrared Sensors (IRIS) that uses no magnetometers (when both sets of magnetometers fail).

The performance of the existing lateral control system of PATH that uses a lead-lag controller is evaluated in simulations on a simplified linear model (the bicycle model) and a complex nonlinear model. Several scenarios are tested: no magnetometer fault, front magnetometer fault, and rear magnetometer fault. These simulations show that although the fixed lead-lag controller works successfully under no fault, it does not provide adequate performance when rear magnetometers fail. More importantly, the lateral control system with this fixed lead-lag controller is unstable when front magnetometers fail.

Since failure of either set of magnetometers leads to degraded operation and can potentially be a safety hazard, new lateral controllers are required to stabilize the system and to improve the performance. Since the vehicle lateral dynamics is observable from the output of either front or rear magnetometers, an observer can be added to complement the information loss caused by the failed magnetometers. Simulations show that this new controller (an observer plus the lead-lag controller) does work. However, this structure is by no means optimal, and the controller has a relatively high order. A more efficient way is to apply H_∞ optimal control theory to the controller design. In the formulation of the H_∞ optimal problem, both the road curvature and the sensor noise are treated as disturbances, and the lateral error and the control force (steering input δ) are treated as errors. Certain weighting functions are chosen to characterize disturbances and to specify the performance requirements. The controller is designed so that the H_∞ norm of the transfer function from the normalized disturbances to the normalized errors is minimized. Two controllers are designed, one based on the output of front magnetometers and the other based on the output of rear magnetometers. Simulations are conducted with these two controllers.

When both sets of magnetometers fail, the controlled vehicle has no direct measurements relative to the road. In this case, a possible backup scheme is to let the controlled vehicle follow its preceding vehicle. This vehicle following control scheme is referred to as the Autonomous Lateral Control (ALC). Certain similarities exist in the control strategies for ALC and those for road-following control. Existing road-following control algorithms can also be applied to ALC as long as the trajectory of the preceding vehicle is determined. When the distance between the two vehicles is small, the trajectory of the preceding vehicle can be assumed to be a straight line within that short distance. The relative lateral deviation and yaw angle of the controlled vehicle with respect to the ideal trajectory are computed according to the geometry in IRIS configurations. Theoretically, if many vehicles in a platoon are under autonomous lateral control, tracking errors will be accumulated on the following vehicles. Namely, the string stability problem of the platoon will occur. This problem may be solved by using an integrated vehicle lateral controller to combine the information from IRIS and the front or rear set of magnetometers. The performance of the integrated control scheme is discussed in this report.

This report is organized as follows. In Section 2, the performance of the lead-lag controller under fault in either the front or the rear set of magnetometers is evaluated, and simulation results on both the bicycle model and the complex nonlinear model are presented. In Section 3, a frequency domain analysis of the vehicle lateral control system under fault is conducted, and H_∞ based lateral controllers are developed to optimize the performance of the control system that uses only one set of magnetometers. In Section 4, autonomous lateral control is studied for the case where the vehicle loses information from both the front and rear sets of magnetometers. In addition, an integrated controller with IRIS and the rear set of magnetometers is developed. In Section 5, conclusions of this report are presented.

2 Vehicle Lateral Control System under Fault

2.1 Introduction

The performance of an existing vehicle lateral control system is evaluated by using both a linearized and a complex nonlinear vehicle model. The linearized model retains lateral and yaw motions of the vehicle's sprung mass, and neglects roll, pitch, vertical motion, and longitudinal acceleration[1][9]. It is usually referred to as the bicycle model. Most of existing lateral control algorithms were designed using the bicycle model, with the road curvature treated as a disturbance. The complex nonlinear model retains more degrees of freedom. This allows for a more precise mathematical representation of the vehicle lateral dynamics. Simulation results using the complex nonlinear vehicle model should be closer to the results obtained from real experiments. However, compared to the complex nonlinear model, the bicycle model is more convenient for system analysis and controller design. The soundness of using a bicycle model for system analysis and controller design can be evaluated by comparing simulation results using the two different vehicle models under the same conditions.

This section is organized as follows. Section 2.2 describes the vehicle models used in the simulation of the existing vehicle lateral control system with a lead/lag controller. Section 2.3 presents simulation results of the control system under different magnetometer failure conditions. A summary is presented in Section 2.4.

2.2 Vehicle Modeling

Vehicle lateral dynamics have been studied since late 1950's. Segel (1956) [8] developed a three-degree-of freedom vehicle model to describe the vehicle directional responses, which includes the yaw, lateral and roll motions. Most of previous research works on vehicle lateral control have relied on the bicycle model that retains only lateral and yaw motions. Vehicle models with more degree-of-freedoms were developed by Lugner (1977)[3], and Peng and Tomizuka (1990)[7]. The first part of this section describes the bicycle model. This is followed by the derivation of a complex nonlinear model. Both models are used in the simulation of the vehicle lateral control system.

2.2.1 Bicycle Model

The simplified control model for passenger vehicles with front wheel steering in Hingwe and Tomizuka (1997)[2] is based on the following assumptions:

- There is no roll, pitch or bounce.
- The relative yaw between vehicle and the road is small.
- The steering angle is small.
- The tire lateral force varies linearly with the slip angle.

Based on the above assumptions, the following simplified model is obtained:

$$m\ddot{y} = -m\dot{\epsilon}\dot{x} - \frac{C_{\alpha_r}(\dot{y} - \dot{\epsilon}l_2)}{\dot{x}} - \frac{C_{\alpha_f}(\dot{y} + \dot{\epsilon}l_1)}{\dot{x}} + C_{\alpha_f} \tag{1}$$

$$I_z\ddot{\epsilon} = l_2\frac{C_{\alpha_r}(\dot{y} - \dot{\epsilon}l_2)}{\dot{x}} - l_1\frac{C_{\alpha_f}(\dot{y} + \dot{\epsilon}l_1)}{\dot{x}} + l_1C_{\alpha_f} \tag{2}$$

where $\dot{x}$ and $\dot{y}$ are components of the vehicle velocity along longitudinal and lateral principle axis of the vehicle body, $\dot{\epsilon}$ is yaw rate, m and I_z are the mass and the yaw moment of inertia, respectively, l_1 and l_2 are respectively distances of the front and rear axle from CG, C_{α_f} and C_{α_r} represent the front and rear tire cornering stiffness, respectively, and δ denotes the steering angle in radian. The equations of the vehicle dynamics can also be written as,

$$\ddot{y_s} = f_1 + b_1\delta \tag{3}$$

$$\begin{aligned}\ddot{\epsilon_r} = {} & \frac{l_1C_{\alpha_f} - l_2C_{\alpha_r}}{I_z\dot{x}}\dot{y_s} + \frac{l_1C_{\alpha_f} - l_2C_{\alpha_r}}{I_z}\epsilon_r + \frac{C_{\alpha_f}l_1}{I_z}\delta - \\ & -\frac{C_{\alpha_f}({l_1}^2 - l_1d_s) + C_{\alpha_r}({l_2}^2 + l_2d_s)}{I_z\dot{x}}\dot{\epsilon_r} - \frac{C_{\alpha_f}{l_1}^2 + C_{\alpha_r}{l_2}^2}{I_z\dot{x}}\dot{\epsilon_d}\end{aligned} \tag{4}$$

where d_s is the distance between the measurement point and the vehicle CG, y_s represents the vehicle lateral error at the measurement point (either real or virtual), ϵ_r is the relative yaw angle, and f_1 and b_1 are given as follows.

$$f_1 = -\frac{\phi_1 + \phi_2}{\dot{x}}\dot{y_s} + (\phi_1 + \phi_2)\epsilon_r + \frac{\phi_1(d_s - l_1) + \phi_2(d_s + l_2)}{\dot{x}}\dot{\epsilon_r} + \frac{\phi_2l_2 - \phi_1l_1 - \dot{x}^2}{\dot{x}}\dot{\epsilon_d} \tag{5}$$

$$b_1 = \phi_1 \tag{6}$$

$$\phi_1 = C_{\alpha_f}(\frac{1}{m} + \frac{l_1 d_s}{I_z}) \tag{7}$$

$$\phi_2 = C_{\alpha_r}(\frac{1}{m} - \frac{l_2 d_s}{I_z}) \tag{8}$$

The state-space-form representation of these equations is

$$\dot{\xi} = A\xi + B\delta + W\rho \tag{9}$$

where

$$\xi = \begin{pmatrix} y_s & \dot{y_s} & \epsilon & \dot{\epsilon} \end{pmatrix}^T \tag{10}$$

$$A = \begin{pmatrix} 0 & 1 & 0 & 0 \\ 0 & -\frac{a_{11}}{\dot{x}} & a_{11} & \frac{a_{12}}{\dot{x}} \\ 0 & 0 & 0 & 1 \\ 0 & -\frac{a_{41}}{\dot{x}} & a_{41} & \frac{a_{42}}{\dot{x}} \end{pmatrix} \tag{11}$$

$$B = \begin{pmatrix} 0 \\ b_{21} \\ 0 \\ b_{41} \end{pmatrix} \tag{12}$$

$$W = \begin{pmatrix} 0 \\ w_{21} \\ 0 \\ w_{41} \end{pmatrix} \tag{13}$$

$$a_{11} = (\phi_1 + \phi_2), a_{12} = \phi_1(d_s - l_1) + \phi_2(d_s + l_2) \tag{14}$$

$$a_{41} = \frac{l_1 C_{\alpha_f} - l_2 C_{\alpha_r}}{I_z} \tag{15}$$

$$a_{42} = \frac{l_1 C_{\alpha_f}(d_s - l_1) + l_2 C_{\alpha_r}(d_s + l_2)}{I_z} \tag{16}$$

$$b_{21} = \phi_1, b_{41} = \frac{l_1 C\alpha_f}{I_z} \tag{17}$$

$$w_{21} = -\frac{{l_1}^2 C_{\alpha_f} + {l_2}^2 C_{\alpha_r}}{I_z} \tag{18}$$

$$w_{41} = \phi_2 l_2 - \phi_1 l_1 - \dot{x}^2 \tag{19}$$

and $\rho = \frac{\dot{\epsilon}_d}{\dot{x}}$ is the road curvature, which is treated as a disturbance in most lateral controller designs.

2.2.2 Complex Model

The complex model used in this report has 6 degrees of freedom, namely,

- x: longitudinal displacement of vehicle CG
- y: lateral displacement of vehicle CG
- z: vertical displacement of vehicle CG
- ϕ: roll angle of the sprung mass
- θ: pitch angle of the sprung mass
- ϵ_r: relative yaw angle of the sprung mass

There are 11 state variables in this model: x, y, $\dot{y}$, z, $\dot{z}$, ϕ, $\dot{\phi}$, θ, $\dot{\theta}$, ϵ_r, and $\dot{\epsilon_r}$. $\dot{x}$ is assumed to be known from longitudinal control, and it is not a state variable. The governing differential equations are borrowed from Hingwe and Tomizuka(1997):

$$m(\ddot{y} + \dot{x}\dot{\epsilon_d}) = \sum_{i=1}^{4} F_{yi}\cos(\epsilon_r) + \sum_{i=1}^{4} F_{xi}\sin(\epsilon_r) \tag{20}$$

$$m\ddot{z} = \sum_{i=1}^{4} F_{zi} - mg \tag{21}$$

$$\begin{aligned}
\ddot{\phi} - \ddot{\epsilon}\sin\theta &= \dot{\theta}\dot{\epsilon}\cos\theta + \frac{M_x^s}{I_x} \\
&\quad - \frac{I_z - I_y}{I_x}(\dot{\epsilon}\sin\phi\cos\theta + \dot{\theta}\cos\phi)(\dot{\epsilon}\cos\phi\cos\theta - \dot{\theta}\sin\phi) \qquad (22) \\
\ddot{\theta}\cos\phi + \ddot{\epsilon}\sin\phi\cos\theta &= \dot{\theta}\dot{\phi}\sin\phi - \dot{\phi}\dot{\epsilon}\cos\phi\cos\theta + \dot{\epsilon}\dot{\theta}\sin\phi\sin\theta + \frac{M_y^s}{I_y} \\
&\quad - \frac{I_x - I_z}{I_y}(\dot{\phi} - \dot{\epsilon}\sin\theta)(\dot{\epsilon}\cos\phi\cos\theta - \dot{\theta}\sin\phi) \qquad (23) \\
\ddot{\epsilon}\cos\phi\cos\theta - \ddot{\theta}\sin\phi &= \dot{\epsilon}\dot{\phi}\sin\phi\cos\theta + \dot{\epsilon}\dot{\theta}\cos\phi\sin\theta + \dot{\phi}\dot{\theta}\cos\phi + \frac{M_z^s}{I_z} \\
&\quad - \frac{I_y - I_x}{I_z}(\dot{\phi} - \dot{\epsilon}\sin\theta)(\dot{\epsilon}\sin\phi\cos\theta - \dot{\theta}\cos\phi) \qquad (24)
\end{aligned}$$

where

- ϵ_d: road curvature
- F_{xi}, F_{yi}, F_{zi}: i-th tire force along x, y, z directions
- M_x^s, M_y^s, M_z^s: moments applied to the sprung mass in x, y, z directions of the sprung coordinate system
- I_x, I_y, I_z: moments of inertia of the sprung mass along x, y, z directions

$\sum_{i=1}^4 M_x^s$, $\sum_{i=1}^4 M_y^s$, $\sum_{i=1}^4 M_z^s$, and $\sum_{i=1}^4 F_{zi}$ are computed according to Peng and Tomizuka (1990). It should be noted that, in Peng and Tomizuka (1990), the definitions of angle variables are different from what we have been using in this report. However, it can be proved that the differences are negligible when these angles are small.

$$
\begin{aligned}
M_x^u &= (\frac{s_{b1}}{2} + h_2\phi)F_{z1} + (\frac{s_{b2}}{2} + h_2\phi)F_{z3} - (\frac{s_b 2}{2} - h_2\phi)F_{z2} - (\frac{s_{b2}}{2} - h_2\phi)F_{z4} \\
&\quad + (z - h_5\theta)\sum_{i=1}^{4} F_{yi} \qquad (25) \\
M_y^u &= (l_2 + h_4\theta)(F_{z3} + F_{z4}) - (l_1 - h_4\theta)(F_{z1} + F_{z2}) - (z - h_5\theta)\sum_{i=1}^{4} F_{xi} \qquad (26) \\
M_z^u &= (l_1 - h_4\theta)(F_{y1} + F_{y2}) - (l_2 + h_4\theta)(F_{y3} + F_{y4}) - (\frac{s_{b1}}{2} + h_2\phi)F_{x1} \\
&\quad - (\frac{s_{b2}}{2} + h_2\phi)F_{x3} + (\frac{s_1}{2} - h_2\phi)F_{x2} + (\frac{s_{b2}}{2} - h_2\phi)F_{x4} \qquad (27)
\end{aligned}
$$

$$F_{zi} = \frac{mgl_2}{2(l_1 + l_2)} + P_{Di} + P_{Fi}, i = 1, 2 \qquad (28)$$

$$F_{zi} = \frac{mgl_1}{2(l_1 + l_2)} + P_{Di} + P_{Fi}, i = 3, 4 \qquad (29)$$

where

$$P_{Di} = D_i\bar{W} + \bar{D}_i(\dot{e}_i - \bar{W}), \dot{e}_i \geq \bar{W} \qquad (30)$$

$$P_{Di} = -D_i\bar{W} + \bar{D}_i(\dot{e}_i + \bar{W}), \dot{e}_i \leq -\bar{W} \qquad (31)$$

$$e_1 = z_0 - z + h_5\theta + l_1\theta - \frac{s_{b1}}{2}\phi \qquad (32)$$

$$e_2 = z_0 - z + h_5\theta + l_1\theta + \frac{s_{b1}}{2}\phi \qquad (33)$$

$$e_3 = z_0 - z + h_5\theta - l_2\theta - \frac{s_{b2}}{2}\phi \qquad (34)$$

$$e_4 = z_0 - z + h_5\theta - l_2\theta + \frac{s_{b2}}{2}\phi \qquad (35)$$

$$P_{Fi} = C_{1i}(e_i + C_{2i}e_i^5), i = 1, 2, 3, 4 \qquad (36)$$

where

- s_{b1} (s_{b2}): distance between the two front (rear) tires
- h_2: vertical distance from CG to the roll center
- h_4 (h_5): vertical (longitudinal) distance from CG to the pitch center
- z_0: the original height of the mass center from the ground
- e_i: spring deflections at the i-th wheel
- P_{Fi}: spring force at the i-th wheel
- P_{Di}: damping force at the i-th wheel
- C_{1i}, C_{2i}: spring constants
- D_i, $\bar{D}_i$: damping coefficients
- $\bar{W}$: limit on deflection rates
- C_{1i}, C_{2i}: cornering stiffness of front and rear tires
- M_x^u, M_y^u, M_z^u: moments applied on the sprung mass in x, y, z directions of the unsprung coordinate system

M_x^s, M_y^s, and M_z^s can be computed by:

$$M_x^s = M_x^u - \theta M_z^u \tag{37}$$

$$M_y^s = M_y^u + \phi M_z^u \tag{38}$$

$$M_z^s = \theta M_x^u - \phi M_y^u + M_z^u \tag{39}$$

To calculate the tire forces F_{xi} and F_{yi}, a linear tire model is used. Let F_{ai} and F_{bi} represent the i-th tire forces which are parallel and normal respectively to the tire plane. Then,

$$F_{bi} = C_{\alpha_i}(\delta - \xi_i) \tag{40}$$

where

$$\xi = \arctan \frac{\dot{y}^u \pm l_i \dot{\epsilon}}{\dot{x}^u} \tag{41}$$

and

$$\dot{x}^u \approx \dot{x}, \dot{y}^u \approx \dot{y} - \dot{x}\epsilon_r \tag{42}$$

From geometry,

$$F_{xi} = F_{ai} \cos \delta_i - F_{bi} \sin \delta_i \tag{43}$$

$$F_{yi} = F_{bi} \cos \delta_i + F_{ai} \sin \delta_i \tag{44}$$

Now we make the following assumptions:

$$F_{a3} + F_{a4} = 0, \delta_1 = \delta_2 = \delta, \delta_{3,4} = 0 \tag{45}$$

These assumptions are reasonable for front wheel steering passenger vehicles. Then from the above equations,

$$\sum_{i=1}^{4} F_{xi} = (F_{a1} + F_{a2}) \cos \delta - (F_{b1} + F_{b2}) \sin \delta \tag{46}$$

$$\sum_{i=1}^{4} F_{yi} = (F_{b1} + F_{b2}) \cos \delta + (F_{a1} + F_{a2}) \sin \delta \tag{47}$$

The only unknown term $(F_{a1} + F_{a2})$ in the above equation can be computed according to the Newtonian dynamic equation along x direction

$$m(\ddot{x} - \dot{y}\dot{\epsilon_d}) = \sum_{i=1}^{4} F_{xi} \cos(\epsilon_r) - \sum_{i=1}^{4} F_{yi} \sin(\epsilon_r) \tag{48}$$

Symbols	Simulation Value	Symbols	Simulation Value
m	$1485Kg$	g	$9.8m/s^2$
d_s	$3m$	I_x	$479.6Kgm^2$
I_y	$2594.3Kgm^2$	I_z	$2872Kgm^2$
l_1	$1.034m$	l_2	$1.491m$
d_1	$1.96m$	d_2	$2.1m$
s_{b1}	$1.45m$	s_{b2}	$1.45m$
z_0	$0.487m$	h_2	$0.3m$
h_4	$0.25m$	h_5	$0.1m$
D, $\bar{D}$	$1500N-s/m$	$\bar{W}$	$0.025m/s$
$C_{\alpha f}$	$40000N/rad)$	$C_{\alpha r}$	$40000N/rad$
C_1	$17000N/m$	C_2	$400001/m^4$

Table 1: Simulation Parameters

2.3 Simulations

Using the vehicle models described in Section 2.2, simulation analysis has been conducted on an existing vehicle lateral control system subject to different magnetometer fault conditions. These conditions are: no magnetometer failure, failure in front magnetometers, and failure in rear magnetometers. Same simulation settings have been applied to both the linearized and complex nonlinear vehicle models in order to compare the results using the two different models.

2.3.1 Settings

Simulation parameters are given in Table 1. The linear controller (being evaluated) is a lead-lag controller with a roll-off at high frequencies for noise reduction: i.e.

$$C(s) = \frac{(s+0.934)(s+0.0934)}{(s+13.1)(s+0.0021)} \frac{10000}{s^2+120s+10000} \tag{49}$$

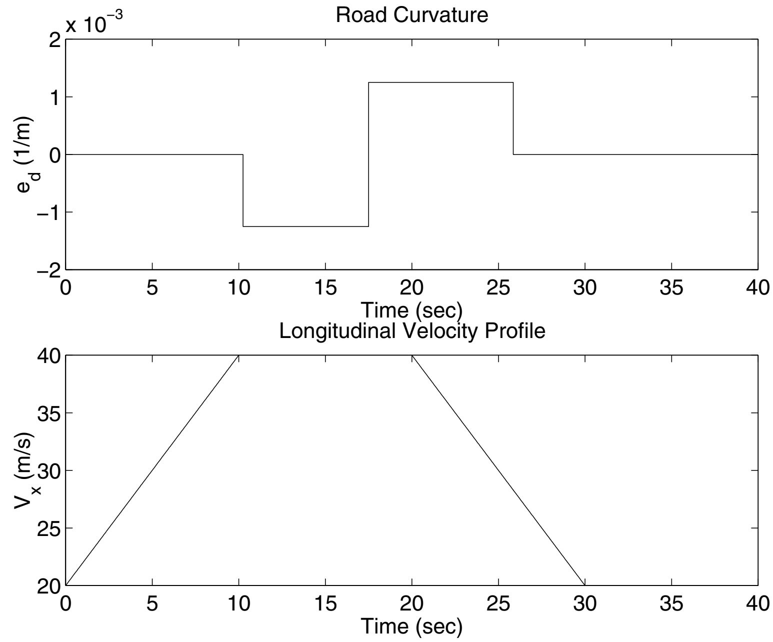

Figure 1: Road curvature and vehicle longitudinal velocity profiles for simulations

The outputs of the front and rear sets of magnetometers are combined to synthesize the lateral error at the virtual sensing point, d_s ahead of the vehicle CG: i.e.

$$y_{vs} = \frac{y_{sf} d_2 + y_{sr} d_1}{d_1 + d_2} + \frac{(y_{sf} - y_{sr}) d_s}{d_1 + d_2} \tag{50}$$

where y_{sf} and y_{sr} denote the outputs from the front and rear magnetometers, respectively. d_1 and d_2 denote the distances from the front and rear sensors to the vehicle CG, respectively. The road curvature and longitudinal velocity profiles used in the simulations are shown in Fig. 1. The vehicle first enters a section with a constant curvature of $-\frac{1}{800} rad/m$, then it enters another curved section with a road curvature of $\frac{1}{800} rad/m$. The longitudinal velocity is first increased gradually from 20 m/sec to 40 m/sec. Then, after 10 sec, it is reduced gradually to 20 m/sec.

2.3.2 Vehicle Lateral Control without Magnetometer Fault

The simulation results of the vehicle lateral control system with no magnetometer fault are shown in Fig. 2. Information from both the front and the rear magne-

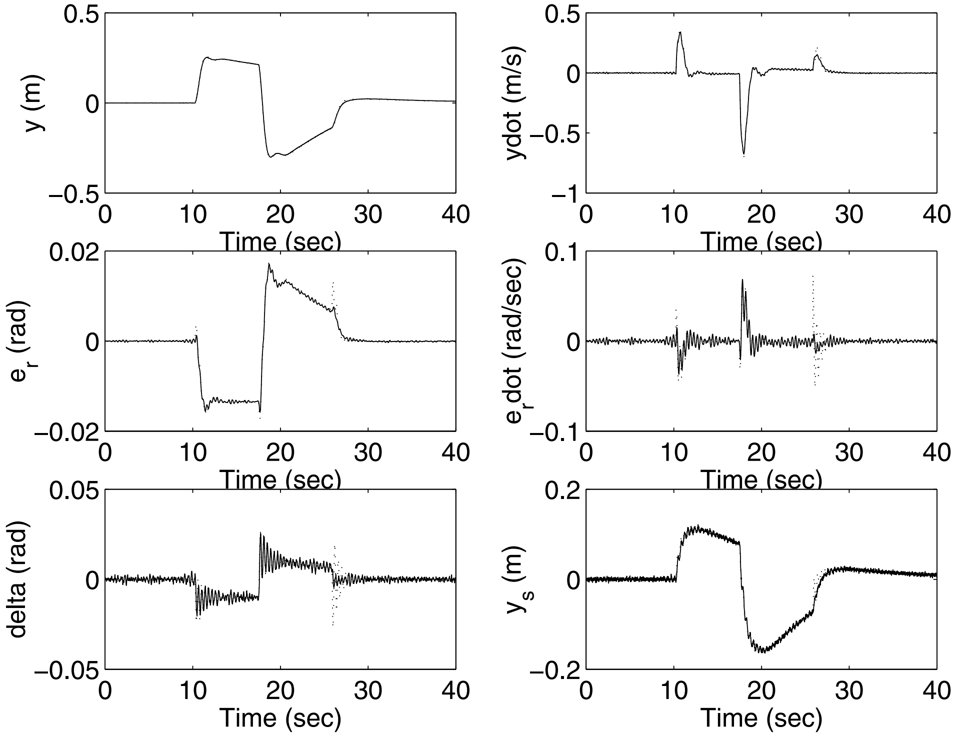

Figure 2: Simulation results of vehicle lateral control without sensor faults (doted: complex model; solid: linear model)

tometers is available to the control system during the simulation. The dotted line represents the results generated by the complex model. The solid line denotes the results generated by the linearized model. The results show that the transient errors generated by the complex model are larger than those generated by the linearized model. There are also more oscillations associated with the system responses produced by the complex model. Apart from these, simulation results from the two models are almost identical. The maximum lateral deviation is about 25 cm for both the linearized and complex vehicle models.

2.3.3 Vehicle Lateral Control with Fault in Rear Magnetometers

When the magnetometers fail, their output may be set by the control logic. In this report, the output of the failed magnetometer is set zero. Figure 3 shows simulation

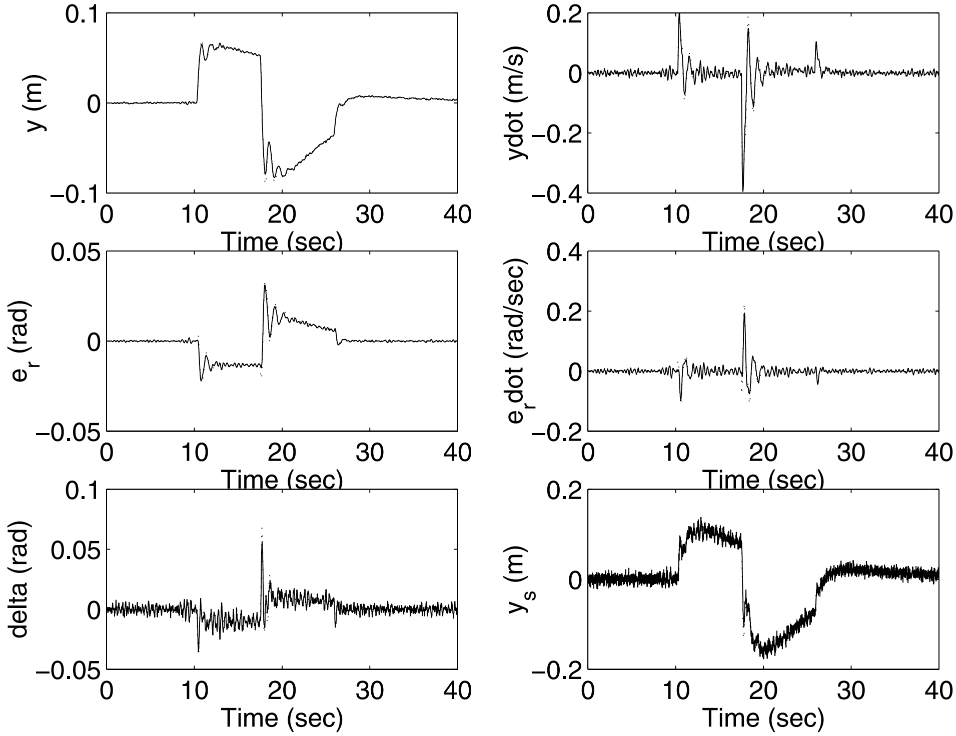

Figure 3: Simulation results of vehicle lateral control with faults in rear sensors (doted: complex model; solid: linear model)

results of the vehicle lateral control system with fault in the rear set of magnetometers. Again, results from both the linearized and the complex nonlinear models indicate similar characteristics. System responses are not as smooth as those in the results with no magnetometer failures. But the vehicle still follows the road centerline reasonably well. The maximum lateral deviation from the road centerline is about 8 cm. The decrease in lateral deviation is caused by the increase of the controller gain. This is concluded by examining the look-ahead scheme in Eq. 50. In this equation, set $y_{sr} = 0$. Since $d_s > d_1$, y_{vs} increases when the rear magnetometers fail. Compared to the results generated by the complex model, the results produced by the linearized model are smoother. Figure 4 shows the transient effects of the failure in rear magnetometers. The rear magnetometers fail suddenly 15 sec after the simulations start. It is assumed that the failure detection algorithm is in place. Failure detection itself

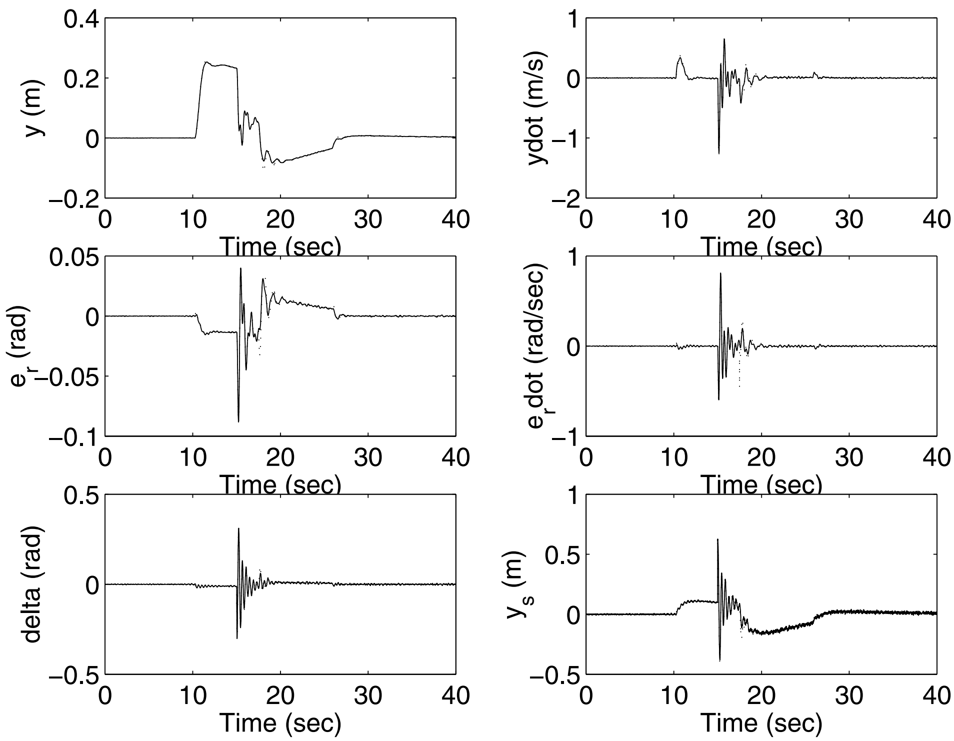

Figure 4: Simulation results of vehicle lateral control with faults in rear sensors after 15 sec (doted: complex model; solid: linear model)

is outside the scope of this report. These plots show that there are large transient errors at the time when the magnetometers fail. But these transient responses settle down in a short time, and the system responses afterwards are similar as those shown in Fig. 3. The simulation results based on both models are similar.

2.3.4 Vehicle Lateral Control with Fault in Front Magnetometers

Under the scenario of front magnetometer failures, simulations indicate instability in the control system. This is because the original look-ahead scheme in Eq. 50 will not work when the front magnetometers fail ($y_{sf} = 0$). However, the system remains observable from the output of the rear set of magnetometers. To estimate the system state variables, a dynamic observer has been designed. A new virtual error at the virtual sensing point is computed according to the estimated state variables.

$$\frac{d}{dt}\begin{bmatrix} x \\ \hat{x} \end{bmatrix} = \begin{bmatrix} A & 0 \\ L_r C_r & A - L_r C_r \end{bmatrix}\begin{bmatrix} x \\ \hat{x} \end{bmatrix} + \begin{bmatrix} B \\ B \end{bmatrix}\delta \tag{51}$$

$$y_{vs} = \begin{bmatrix} 0 & 0 & 0 & 0 & 1 & 0 & d_s & 0 \end{bmatrix}\begin{bmatrix} x \\ \hat{x} \end{bmatrix} \tag{52}$$

where

$$C_r = \begin{bmatrix} 1 & 0 & -l_2 & 0 \end{bmatrix} \tag{53}$$

Simulation results are shown in Fig. 5. There is a significant difference in the results using the two different vehicle models. Results on the linear model show that the system is stable with small oscillations, while results on the complex nonlinear model indicate unacceptable oscillations in the vehicle speed reduction section. Since the complex model is closer to the rear vehicle plant, the performances of the existing control system in the event rear magnetometers fail are not satisfactory.

2.4 Summary

In this section, simulation analysis of the vehicle lateral control system subject to different magnetormeter fault conditions has been conducted. Both the bicycle model and the complex nonlinear vehicle models have been used and compared in simulations. Simulation results show that in general these two models generate similar results, but the results based on the complex nonlinear model are not as smooth as those based on the linearized model. The effects of different magnetometer failures on the vehicle lateral control system are not same. Failures in the rear magnetometers do not affect the system performances significantly, and the vehicle tracks the road centerline at the accuracy of about 8 *cm*, without losing much of smoothness. However, failures in the front magnetometers cause instability in the control system. Using a dynamic state observer may stabilize the system, but the simulation results using the complex model show that the system performances are still not satisfactory.

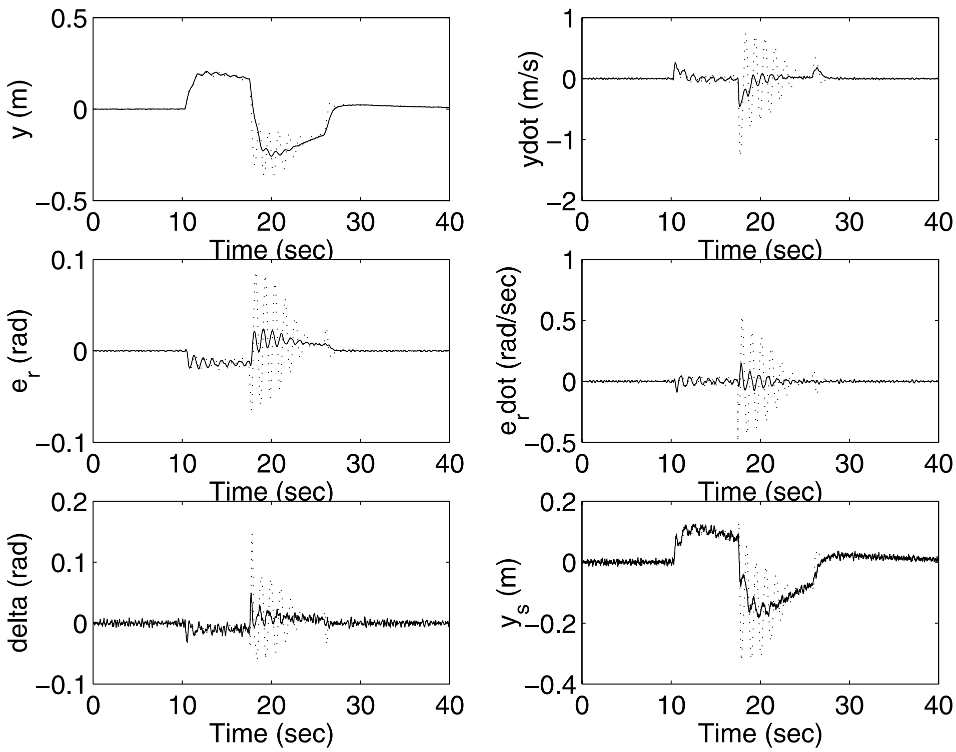

Figure 5: Simulation results of vehicle lateral control with faults in front sensors (doted: complex model; solid: linear model)

3 Controller Design with One Set of Magnetometers

3.1 Introduction

In Section 2, the performance of the vehicle lateral control system with a lead-lag controller was evaluated by simulations for cases with and without fault. Simulations show that: under no fault the fixed lead-lag controller provides adequate performance; under fault in rear magnetometers the lead-lag controller stabilizes the system but the performance deteriorates; and under fault in front magnetometers, the lead-lag controller fails to stabilize the system. This implies that the control system under fault differs significantly from the control system without fault. Hence, the control system under fault demands systematic studies, and new controllers are required to stabilize the system and improve the performance under magnetometer failures.

In this section, vehicle lateral control under fault in one set of magnetometers is analyzed in the frequency domain. Two controllers are designed based on H_∞ optimal control theory, one using the output of front magnetometers and the other using the output of rear magnetometers. Simulations with these two controllers are conducted, and conclusions are given at the end of the section.

3.2 Frequency domain analysis of vehicle lateral control under fault in one set of magnetometers

The current PATH lateral control algorithms employ two sets of magnetometers to implement the virtual look-ahead scheme [5][6]. According to this scheme, a lateral error (called virtual lateral error) at some distance d_s (look-ahead distance) ahead the vehicle is constructed from the outputs of the two sets of magnetometers (front and rear magnetometers). The control objective is to minimize the virtual lateral error. In other words, the virtual look-ahead scheme is trying to minimize the lateral error

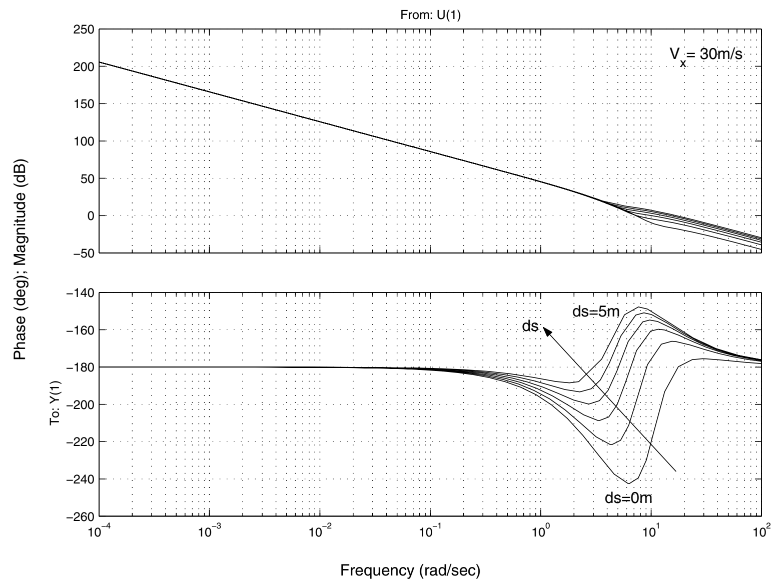

Figure 6: Bode plot of G_v (the TF from the steering input to virtual lateral error)

at some distance ahead the vehicle.

A frequency domain analysis shows that as the look-ahead distance d_s increases the phase lead enhances (Fig. 6). Therefore, large look-ahead distances result in increased phase lead, which significantly eases the controller design. This effect of the look-ahead distance is the main advantage of the virtual look-ahead scheme. However, if magnetometer failures occur, the look-ahead distance decreases to certain fixed values. Under fault in front magnetometers, only the lateral error at the rear magnetometers is available. Thus, the look-ahead distance d_s decreases to $-l_2$ (l_2 is the distance between the mass center and the rear bumper). Similarly, under fault in rear magnetometers, the look-ahead distance decreases to l_1 (the distance between the mass center and the front bumper). In both cases, the look-ahead distance is small and the phase lead in the system is not adequate. Figures 7 and 8 show the frequency responses from the steering input δ to the lateral error at the front bumper y_{sf} and at the rear bumper y_{sr} when the longitudinal velocity is $30m/s$. The decrease of phase lead increases the difficulty in the controller design, especially for the system with front magnetometer failure.

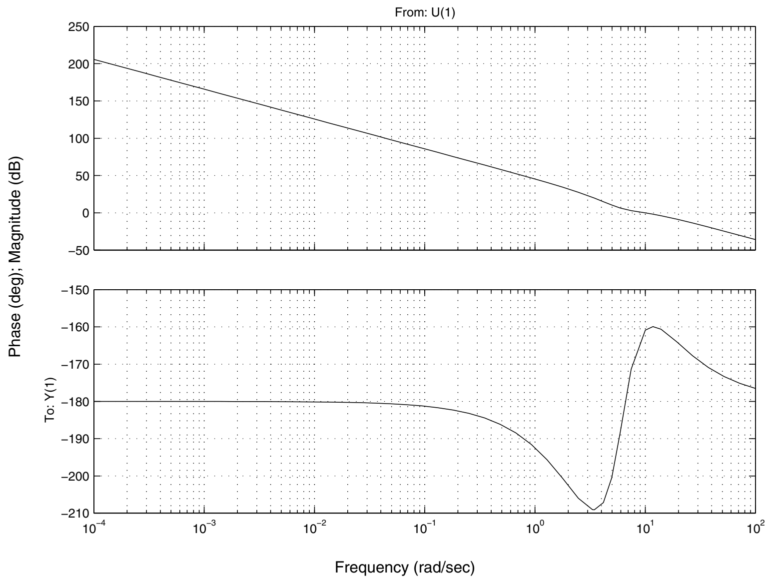

Figure 7: Bode plot of G_f (the TF from the steering input to y_{sf})

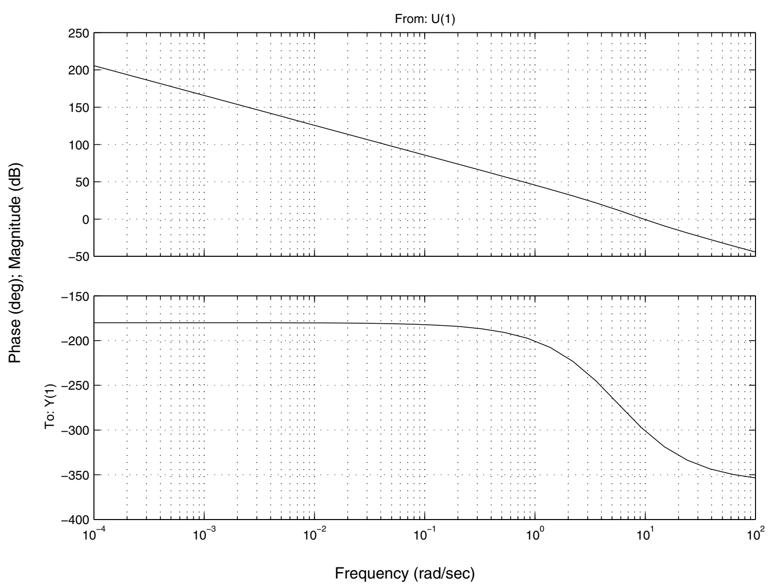

Figure 8: Bode plot of G_r (the TF from the steering input to y_{sr})

Since vehicle lateral dynamics is observable from the output of either the front or the rear set of magnetometers, there exist output feedback controllers that at least stabilize the system. An intuitive idea is to implement the virtual look-ahead scheme by adding an observer; that is, instead of constructing the virtual lateral error from the lateral errors measured by front and rear magnetometers, we estimate the virtual lateral error using the states of the observer. This was done in the previous section and simulations show that it works. However, this approach increases the order of the controller; and the system performance depends on the efficiency of the lead-lag controller which is designed without consideration of road curvature and sensor noises. To avoid these disadvantages, our controller design is based on the H_∞ optimal control technique.

3.3 Controller Design

According to the H_∞ optimal control technique, both the disturbance ($\dot{\epsilon}_d$) and magnetometer noise are regarded as disturbances, while the lateral error and control effort are treated as errors. The formulation of the H_∞ synthesis for the vehicle lateral control system is shown in Fig. 9. G is the vehicle model (see Eq. 1). W_{perf} and W_u are the weighting functions chosen according to the requirements on the lateral error and the limitation on the allowable control input; W_{dist} and W_{noise} model the disturbance ($\dot{\epsilon}_d$) and magnetometer noise. Our objective is to synthesizes a controller K which minimizes the effects of the normalized disturbances (d_N and n_N) on the normalized errors (e_1 and e_2) in the sense of H_∞ norm: i.e.

$$\min \|T_{e \leftarrow d}\|_\infty \tag{54}$$

where d is $[d_N \ n_N]^T$, e is $[e_1 \ e_2]^T$, $T_{e \leftarrow d}$ is the transfer function from d to e.

An important part of the H_∞ synthesis is the normalization of the disturbances and errors. The normalization is a way to specify the performance criterions and model the actual disturbance, the actuator dynamics and measurement noise. The

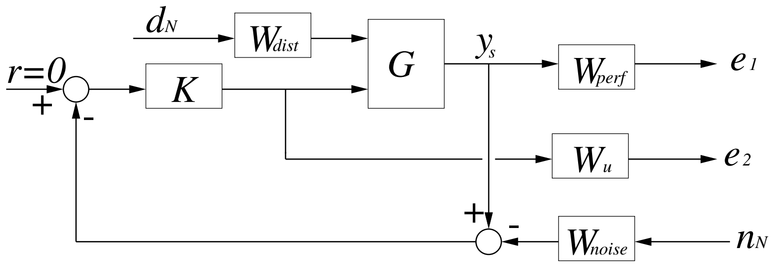

Figure 9: Formulation of H_∞ synthesis

frequency weighting functions used in these normalization are explained below.

- Modeling of the lateral disturbance $\dot{\epsilon}_d$:

  The lateral disturbance $\dot{\epsilon}_d$ in Eq. 1 is given by:

$$\dot{\epsilon}_d = \rho v_x \tag{55}$$

  where ρ is the road curvature, and v_x is the longitudinal velocity. The maximum magnitude of the road curvature is set to be $\frac{1}{800m}$ in the H_∞ synthesis, which is larger than the general curvature on highways. Since the road curvature does not change frequently on highways, the disturbance can be modeled as a band limited signal. To keep the order of the controller small, the disturbance is modeled as a constant.

$$W_{dist} = \frac{v_n}{800} \tag{56}$$

  where v_n is a nominal velocity which can be chosen individually in the synthesis.

- Modeling of magnetometer noise:

  Since noise in the measurement generally has high frequency components, the weighting on noise should be a high pass filter. In consideration of the order of the resulting controller, however, the noise weighting function is chosen to be a constant.

$$W_{noise} = \frac{1}{200} \tag{57}$$

- Penalty on the lateral error y_s:

  The high frequency component of the lateral error measurement is considered as noise. This is because the road curvature is piecewise continuous and the vehicle dynamics contains mainly low frequency dynamics. Thus the penalty is set high on the low frequency components of the lateral error measurement.

$$W_{perf} = 0.2 \frac{s+30}{s+0.03} \tag{58}$$

- Penalty on the steering action:

  The high frequency component of the control input must be restricted because it may saturate the actuator and excite the unmodeled high frequency components. Therefore, the penalty is set high at high frequencies, and the bandwidth of the controller is set to be lower than that of the actuator (which is around 5Hz).

$$W_u = 1400 \frac{s+10}{s+100} \tag{59}$$

The resulting controller has an order equivalent to the sum of the orders of the vehicle model and all the weighting functions. The vehicle model is 4th order, and the sum of the weighting functions' orders is 2. Hence, the resulting controller has an order of 6.

In the controller design, the nominal velocity is set to $20m/s$. The parameters used are from the PATH Test vehicle (Buick LeSabre) (see Table 2). The resulting controllers are as follows:

The control system with front magnetometer:

$$G_{kf} = \frac{-12.3s^5 - 1570s^4 - 3.714 \times 10^4 s^3 - 3.21 \times 10^5 s^2 - 3.68 \times 10^5 s - 2.077 \times 10^5}{s^6 + 127.5s^5 + 5097s^4 + 1.014 \times 10^5 s^3 + 9.858 \times 10^5 s^2 + 4.191 \times 10^6 s + 1.249 \times 10^5} \tag{60}$$

The control system with rear magnetometers:

$$G_{kr} = \frac{-23.28s^5 - 2770s^4 - 4.84 \times 10^4 s^3 - 4.234 \times 10^5 s^2 - 5.485 \times 10^5 s - 3.519 \times 10^5}{s^6 + 159s^5 + 6094s^4 + 1.217 \times 10^5 s^3 + 1.463 \times 10^6 s^2 + 1.043 \times 10^7 s + 3.116 \times 10^5} \tag{61}$$

Symbols	Simulation Value	Symbols	Simulation Value
m	$1740Kg$	g	$9.8m/s^2$
l_1	$1.04m$	l_2	$1.76m$
C_{af}	$70000N/m$	C_{rf}	$1300001/m^4$
I_z	$3214Kgm^2$		

Table 2: Parameters for a Buick car

The resulting controllers are shown in Fig. 10 and Fig. 11. From bode plots we can see that the control system with rear magnetometers provides more phase lead than the one with front magnetometers. This is reasonable since the vehicle has more phase lag if the output is the lateral error under the rear bumper.

3.4 Simulation Results

Simulations are performed with the bicycle model. The profile of the road curvature is shown in Fig. 12. The road curvature changes from 0 to $-1/(800m)$ to $+1/(800m)$ and back to 0. Therefore, the maximum transition curvature is $1/(400m)$ which is much greater than the curvature on highways (less than $1/(1000m)$). The longitudinal velocity is assumed to be constant, and three velocities ($20m/s$, $30m/s$, $35m/s$) are tested. The simulation results of the closed-loop system with front magnetometers are shown in Fig. 13. For road curvature up to $1/(800m)$, the maximum lateral error at $v_x = 20m/s$ is about 5cm, and at $v_x = 35m/s$ is about 10cm. Compared to the simulation results with the lead-lag controller (Fig. 3), the control input is much smoother (the oscillation is smaller), and it is also smaller in magnitude. Figure 14 shows the simulation results of the closed-loop system with rear magnetometers. The lateral error for road curvature $1/800m$ at $v_x = 20m/s$ is about 10cm, which is larger than the error with the front magnetometers, but still much smaller than the allowable error (at road curvature transition $1/1000m$, the error should be less

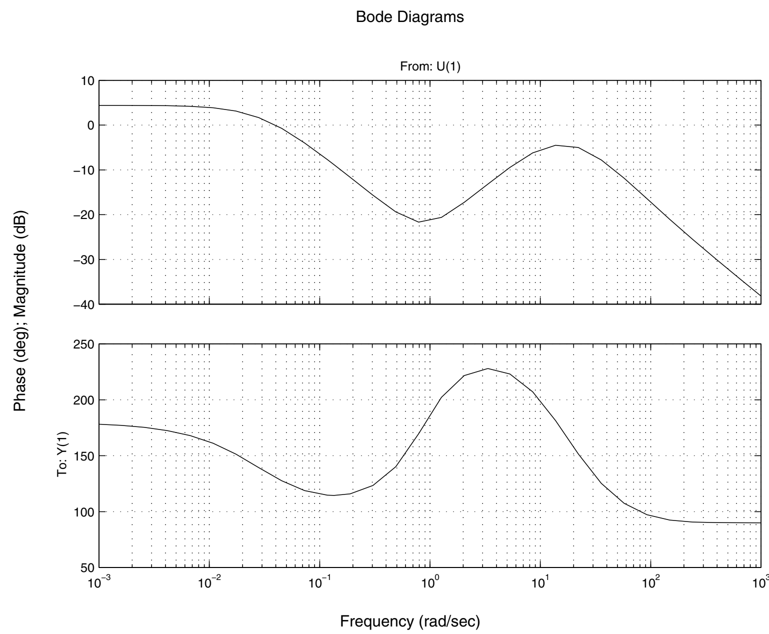

Figure 10: Bode plot of the control system with front magnetometers

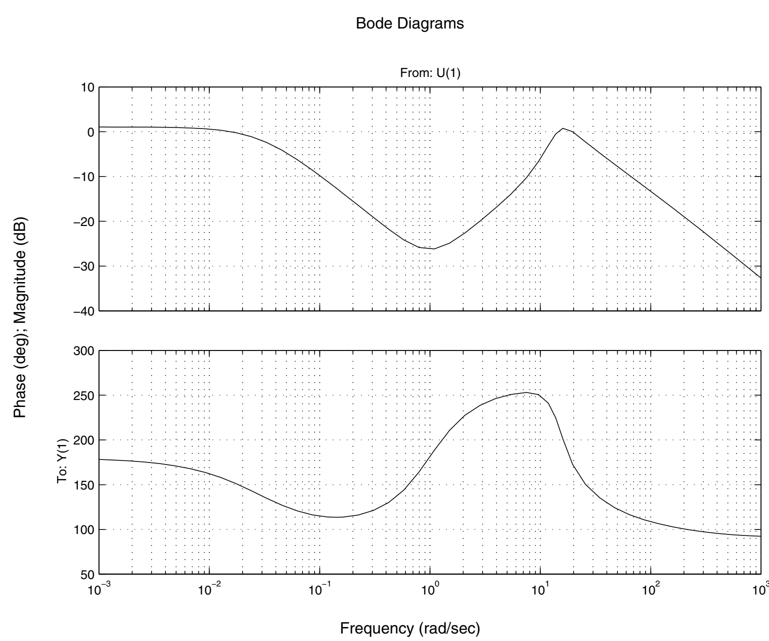

Figure 11: Bode plot of the control system with rear magnetometers

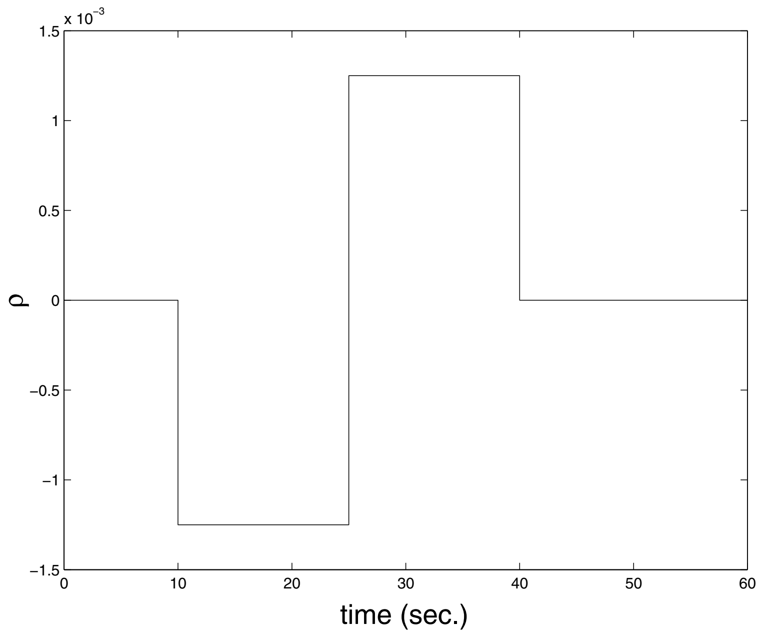

Figure 12: The profile of the road curvature

than 30cm). However, as the velocity increases, the oscillations become more severe. Further investigations are required to reduce the magnitude of the oscillations.

3.5 Summary

In this section, the frequency domain analysis of the vehicle lateral control system under fault in one set of magnetometers was presented. Two controllers were designed based on the H_∞ optimal control technique: one using the output of front magnetometers and the other using the output of rear magnetometers. Simulations with these two controllers show that the control is smooth up to $v_x = 30m/s$, and the lateral error is within the acceptable range.

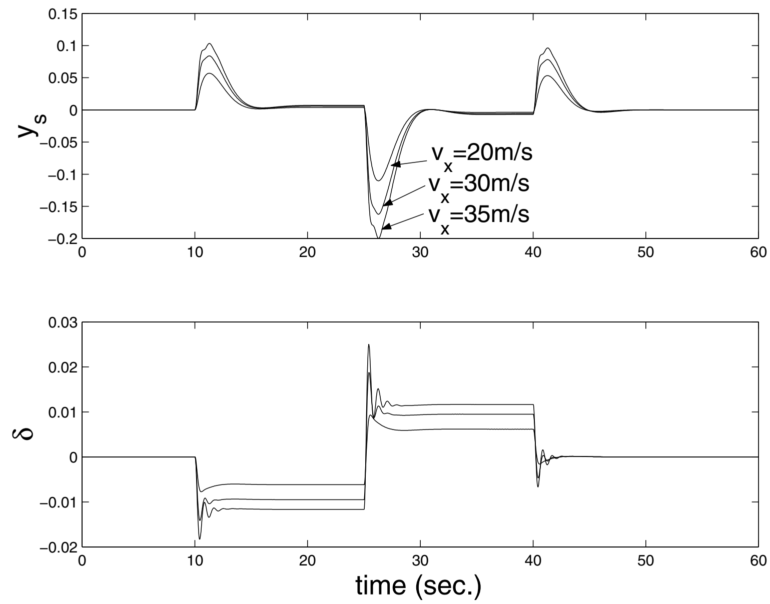

Figure 13: Simulation of the controller with only the front magnetometers

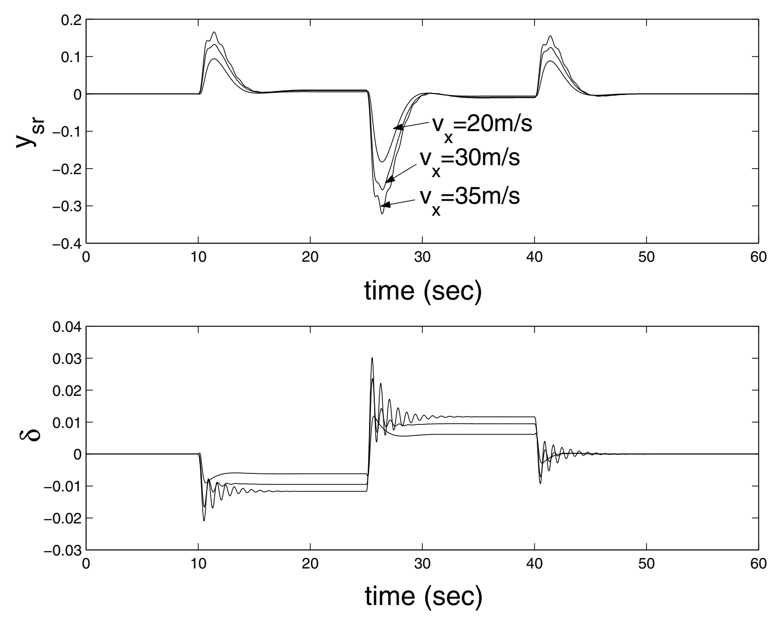

Figure 14: Simulation of the controller with only the rear magnetometers

4 Study of Autonomous Lateral Control

4.1 Introduction

When both front and rear magnetometers fail, there will be no direct measurements for the lateral displacement of the vehicle relative to the road centerline. In this case, the vehicle can be controlled to follow the preceding vehicle, assuming that the preceding vehicle is on the desired track with no lateral error nor relative yaw error with respect to the road centerline. This vehicle-following control algorithm is referred to as the Autonomous Lateral Control (ALC), and it may serve as a back-up system for the magnetometer-based vehicle lateral control scheme in the case of magnetometer failures. In order to control the vehicle to follow the track of the preceding vehicle, ALC requires the measurements of the relative lateral distance and yaw angle between the two vehicles. In this project, they are measured by the Intelligent Ranging using Infrared Sensors (IRIS) developed by researchers of UCLA.

In practice, the preceding vehicle is not necessarily on the desired track. The lateral error and yaw of the preceding vehicle will be passed on to the following vehicle, when the following vehicle follows the track of the preceding one. Since it is impossible for the controlled vehicle to follow the preceding vehicle perfectly, the controlled vehicle will have larger lateral errors than the preceding vehicle. If there are many vehicles under ALC in a platoon, and each of them follows its preceding vehicle except the leading one, the lateral errors of the following vehicles will be accumulated. This may cause the string stability problem of the platoon in the lateral direction.

The string stability problem may be solved by combining the autonomous lateral control scheme with the information from magnetometers. Since magnetometers measure the lateral error of the vehicle with respect to the road centerline, combining ALC with the information from magnetometers will reduce the lateral errors of the following vehicles. Autonomous lateral control may in return improve the robustness and performance of magnetometer-based lateral control systems, especially when the control systems use only rear magnetometers. As described in Section 2, when the front magnetometers fail, the magnet-magnetometer based control only uses the rear magnetometers, and its performance is significantly limited. This is because there are no physical look-ahead measurements in such a case. This problem may be solved by combining this control system with ALC, because IRIS can work as a look-ahead sensor.

The IRIS system is introduced in Section 4.2. It is followed by the design and simulation results for autonomous lateral control in Section 4.3. Section 4.4 presents the idea and simulation results for integrated lateral control which uses ALC along with the information from rear magnetometers. Finally, a summary is presented in Section 4.5.

4.2 Intelligent Ranging with Infrared Sensors(IRIS)

The IRIS system is composed of a low-power infrared diode laser illuminator with a relatively wide beam which is pulsed on/off, and a receiver consisting of a charged-coupled device (CCD) image sensor behind a narrow bandpass filter. The system records two images of the preceding vehicle in rapid succession: the first one with the illumination laser turned off, and the second one with the laser on. Due to the micrometer wavelength of the illuminator, almost all surfaces of the preceding vehicle and the surrounding objects scatter the incident laser beam and reflect only a negligible fraction back to the receiver to be recorded on the second (laser on) image. Some surfaces, however, reflect most of the incident laser beam back to its source. These are the passive reflective patches molded into the taillights of all modern vehicles, as well as the reflective paint used in the license plates of many states, which act as efficient retroreflectors in the illuminator's wavelength. UCLA researchers have demonstrated that subtraction of the first (laser off) image from the second (laser on) one yields a clear sharp image of these reflective surfaces against a flat background. The distance to the preceding vehicle as well as the relative lateral and yaw errors are then easily computed from the resulting clear pattern via standard triangulation schemes.

In order to compute the absolute distance and relative velocity to the preceding vehicle, the IRIS sensor needs to know a base line lateral distance, such as the distance between the taillights of that vehicle. This is due to the fact that IRIS uses triangulation schemes, so at least one of the sides of the triangle needs to be of known length. Since the distance between taillights varies from one vehicle to the next, using one CCD receiver cannot yield accurate absolute distance measurements when used alone in a general highway environment. However, this problem can be eliminated through a straightforward modification of the sensor configuration: instead of using one CCD receiver, one can use two which are mounted at a known lateral distance from each other on the host vehicle. To distinguish between these two configurations, we denote them as IRIS-1 and IRIS-2 depending on whether one or two receivers are used. The IRIS-2 sensor uses the distance between its receivers as the baseline, and then measures the apparent positions of the same object (such as left or right taillight) on each of its two receivers to implement its triangulation schemes. Thus IRIS-2 can compute absolute distance at the additional cost of a second receiver and a more elaborate vehicle installation procedure. Another advantage of IRIS-2 over IRIS-1 is that it can maintain tracking at distances as low as 0.5 meter by appropriately adjusting the orientation of one of its receivers. The geometric scheme of IRIS-2 to calculate the relative lateral error and yaw is shown in Fig. 15. The algorithm to calculate the longitudinal and lateral distances and the yaw of the preceding vehicle can be deduced by using simple geometry. We set up the coordinate with the origin $(0,0)$ at S_r, which corresponds to the lens focus point of the right CCD image sensor. The L_{ll} stands for the geometric line from the left reflective taillight on the back of the preceding vehicle to the focus point of the left CCD sensor installed on the following vehicle. Other lines (L_{lr}, L_{rl}, and L_{rr}) have the same geometric meanings. One can

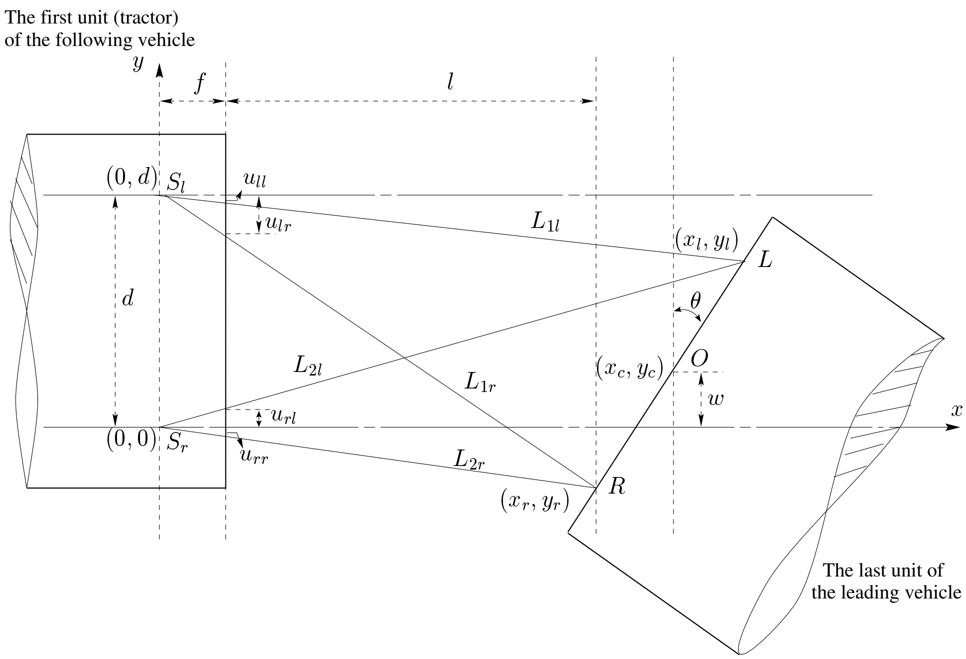

Figure 15: Geometry for IRIS-2 configuration

easily obtain the geometric functions of the lines L_{ll}, L_{lr}, L_{rl}, L_{rr} as

$$L_{ll} : y = d - \frac{f}{u_{1l}} x \tag{62}$$

$$L_{lr} : y = d - \frac{f}{u_{1r}} x \tag{63}$$

$$L_{rl} : y = d - \frac{f}{u_{2l}} x \tag{64}$$

$$L_{rr} : y = d - \frac{f}{u_{2r}} x \tag{65}$$

The intersection point (x_l, y_l) of L_{ll} and L_{rl}, which is the position of the left taillight of the preceding vehicle, is computed as

$$x_l = \frac{u_{ll} u_{rl} d}{f(u_{ll} + u_{rl})} \tag{66}$$

$$y_l = \frac{u_{ll} d}{(u_{ll} + u_{rl})} \tag{67}$$

Similarly, the intersection point (x_r, y_r) of L_{lr} and L_{rr}, which stands for the position of right taillight of the preceding vehicle, is

$$x_l = \frac{u_{lr}u_{rr}d}{f(u_{rr} - u_{lr})} \tag{68}$$

$$y_l = \frac{u_{lr}d}{(u_{rr} - u_{rl})} \tag{69}$$

The yaw is computed as

$$\theta = \arctan(\frac{x_l - x_r}{y_l - y_r}) \tag{70}$$

and the longitudinal and lateral distances (l and w in Fig. 15) are

$$l = min(x_r, x_l) - f \tag{71}$$

$$w = \frac{y_l + y_r}{2} \tag{72}$$

From the computing procedure of longitudinal and lateral distances and the yaw of the preceding vehicle, we can see that IRIS-2 does not require knowledge of the distance between the two taillights of the preceding vehicle, while that knowledge is necessary for IRIS-1. So a vehicle equipped with the IRIS-2 sensor can accurately obtain all the necessary information for longitudinal and lateral control for any type of preceding vehicle, as long as that vehicle has the reflective taillights required by law.

4.3 Autonomous Lateral Control

If the trajectory of the preceding vehicle can be exactly determined, then existing lateral control algorithms for vehicle road following can also be applied to vehicle trajectory following, or alternatively Autonomous Lateral Control (ALC). The only difference is that, under ALC, the controlled vehicle follows the on-line calculated trajectory of the preceding vehicle, instead of the road centerline. This similarity between the two control algorithms allows the proposed ALC, as a back-up system for the magnet-magnetometer based lateral control scheme, to use a similar control structure as that of the original system. Thus, most of existing road-following analysis and algorithms, such as the look-ahead scheme and gain-scheduling techniques, can also be utilized in the development of autonomous lateral control. This will also simplify the implementation of ALC in addition to the original magnetometer-based control system.

when the longitudinal space between the two vehicles is small, it can be assumed that the trajectory of the preceding vehicle is a straight line in that short distance. Similarly as what we did in road following, we can construct a look-ahead scheme for ALC, and use a lead-lag like controller to control the virtual error at the look-ahead distance to remain small during vehicle following. This will result in small tracking errors of vehicle CG with respect to the trajectory of the preceding vehicle. The detailed control methods are as follows.

In section 4.2, we developed algorithms to compute l, w, and θ. We now first relate them to the regulation variables for vehicle lateral control.

$$\Delta y = (w - \frac{d}{2}) - (d_I + l)\theta \tag{73}$$

$$\Delta\epsilon_r = \theta \tag{74}$$

where Δy and $\Delta\epsilon_r$ are the lateral error and yaw relative to the front vehicle as defined in Fig. 16, and d_I is the distance of IRIS from vehicle CG along the longitudinal direction. As indicated in Fig. 16, it is assumed that the trajectory of the preceding vehicle is a straight line within the short distance between the two vehicles. The virtual error at the look-ahead distance of ALC is defined as

$$y_{vs} = \Delta y + \Delta\epsilon_r d_s \tag{75}$$

where d_s is the look-ahead distance. Then, y_{vs} is used as the input to the following

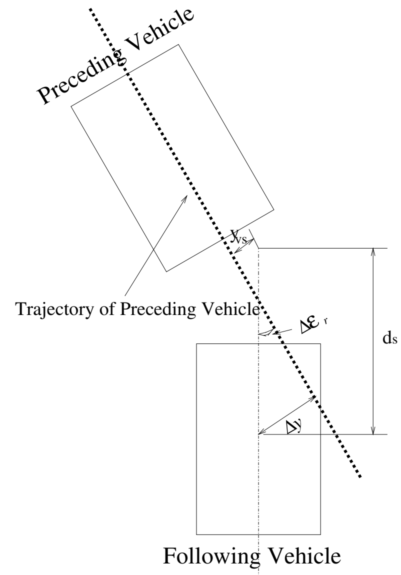

Figure 16: The control scheme of ALC

controller

$$C(s) = \frac{(s + 0.934)(s + 0.0934)}{(s + 13.1)(s + 0.0021)} \frac{10000}{s^2 + 120s + 10000} \tag{76}$$

The output of the controller is the commanded steering angle.

For simulation of ALC, a platoon of three vehicles is assumed, with the two following vehicles under autonomous lateral control. For the lead vehicle, the feedback signals are the measurements from the front and rear magnetometers, while for the following vehicles, they are the relative lateral distance and yaw with respect to the preceding vehicle measured by IRIS. The road curvature, longitudinal velocity profiles, and other simulation settings are same as those in the previous sections. The longitudinal distance between every two adjacent vehicles is set to $3m$. Simulation results are shown in Fig. 17. The results are plotted in the road coordinate system. These figures show that the lateral error of the leading vehicle results in successively larger lateral errors of the following vehicles. The maximum lateral error of the first vehicle is $20cm$, while that of the third vehicle is over $50cm$. The same trend applies to the other variables, $\dot{y}$, ϵ_r, and $\dot{\epsilon}_r$. The leading vehicle's lateral error and yaw relative

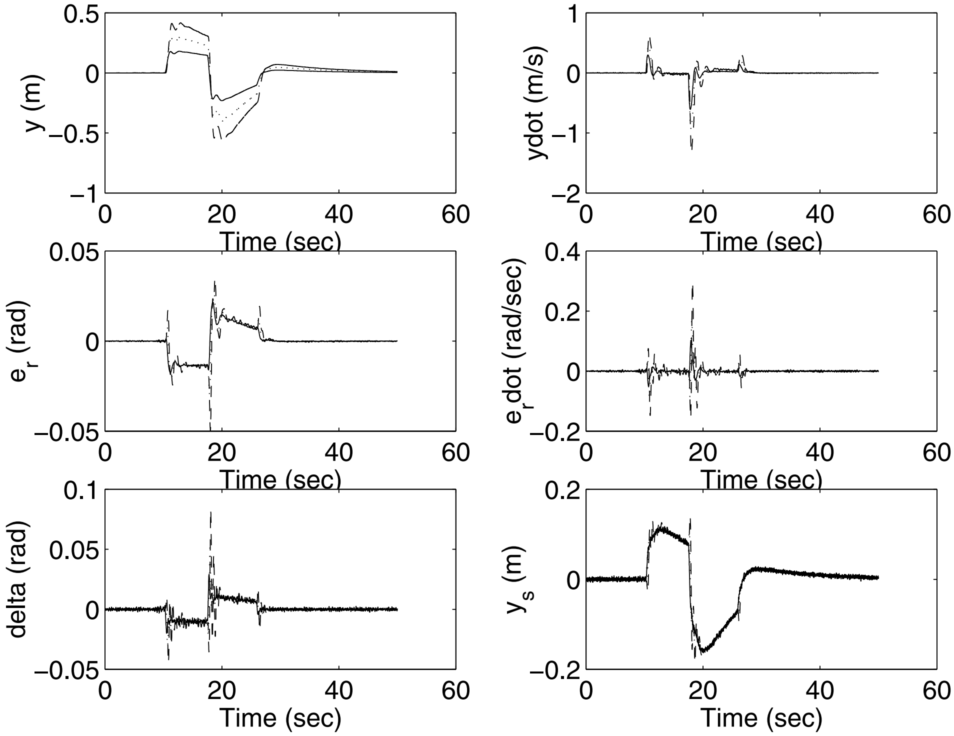

Figure 17: Simulation results for autonomous lateral control (solid: first vehicle; dotted: second vehicle; dashed: third vehicle)

to the road centerline are passed on to all the vehicles which follow it, and result in accumulation of tracking errors of the following vehicles. This may cause a serious problem if many vehicles are under autonomous lateral control in a platoon.

4.4 Integrated Lateral Control with ALC and Rear Sensors

As described in Section 2, the vehicle, as a controlled system, remains observable from the output of the rear magnetometers, under the scenario of the front magnetometer failures. A dynamic state observer has been designed to estimate the system state variables,

$$\frac{d}{dt}\begin{bmatrix} x \\ \hat{x} \end{bmatrix} = \begin{bmatrix} A & 0 \\ L_r C_r & A - L_r C_r \end{bmatrix} \begin{bmatrix} x \\ \hat{x} \end{bmatrix} + \begin{bmatrix} B \\ B \end{bmatrix} \delta \tag{77}$$

$$\hat{y} = C_r x \tag{78}$$

where

$$C_r = \left[\begin{array}{cccc} 1 & 0 & -l_2 & 0 \end{array} \right] \tag{79}$$

$$\hat{x} = \left[\begin{array}{cccc} \hat{y}_{CG} & \dot{\hat{y}}_{CG} & \hat{\epsilon_r} & \dot{\hat{\epsilon_r}} \end{array} \right] \tag{80}$$

The lateral error at the virtual sensor can be computed from the estimated state variables,

$$\hat{y}_{vs} = \hat{y}_{CG} + \hat{\epsilon_r} d_s \tag{81}$$

Under ALC, the virtual error is calculated by assuming that the trajectory of the preceding vehicle is a straight line within short distances, as described in Section 4.3. By combining the virtual errors calculated from the above two different methods, we may construct an integrated control with ALC along with the information from the rear set of magnetometers. Let y_{vs1} denote the virtual error generated by autonomous lateral control scheme, and let y_{vs2} denote the virtual error generated from the estimated state variables using the information from the rear magnetometers: i.e.

$$y_{vs1} = \Delta y + \Delta \epsilon_r d_s \tag{82}$$

$$y_{vs2} = \hat{y}_{CG} + \hat{\epsilon_r} d_s \tag{83}$$

The new virtual lateral error for the integrated controller is defined as

$$y_{vs} = \frac{y_{vs1} + y_{vs2}}{2} \tag{84}$$

The lead-lag like controller in Eq. (76) is used to regulate y_{vs}. The control scheme is shown in Fig. 18, where K is the controller described in Eq. (76), and

$$L_s = \left[\begin{array}{cccc} 1 & 0 & d_s & 0 \end{array} \right] \tag{85}$$

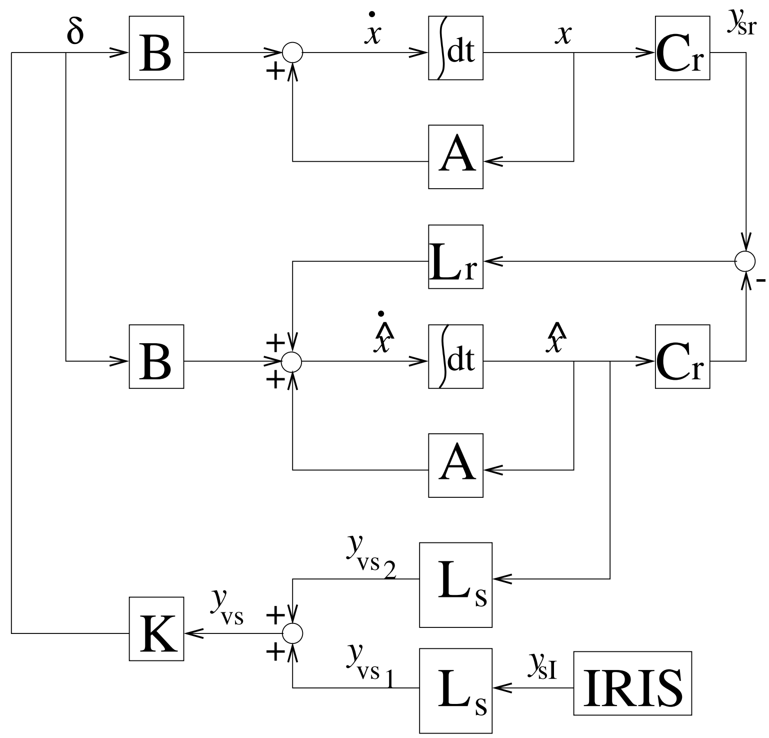

Figure 18: The integrated lateral control scheme

$$y_{sI} = \begin{bmatrix} \Delta y \\ 0 \\ \Delta \epsilon_r \\ 0 \end{bmatrix} \tag{86}$$

This method utilizes lateral and yaw information provided by the IRIS system and the rear magnetometers. The information from the two sources are equally weighted at the current time. The search for the optimal weighting factors for them is a future research topic. The simulation results are shown in Fig. 19. The results indicate a tradeoff between tracking accuracy and smoothness when the information from the rear magnetometers is used along with IRIS. The lateral errors of the following vehicles are much smaller compared to the results shown in Fig. 17, which uses the information from IRIS alone. Compared to the results shown in Section 2, which uses

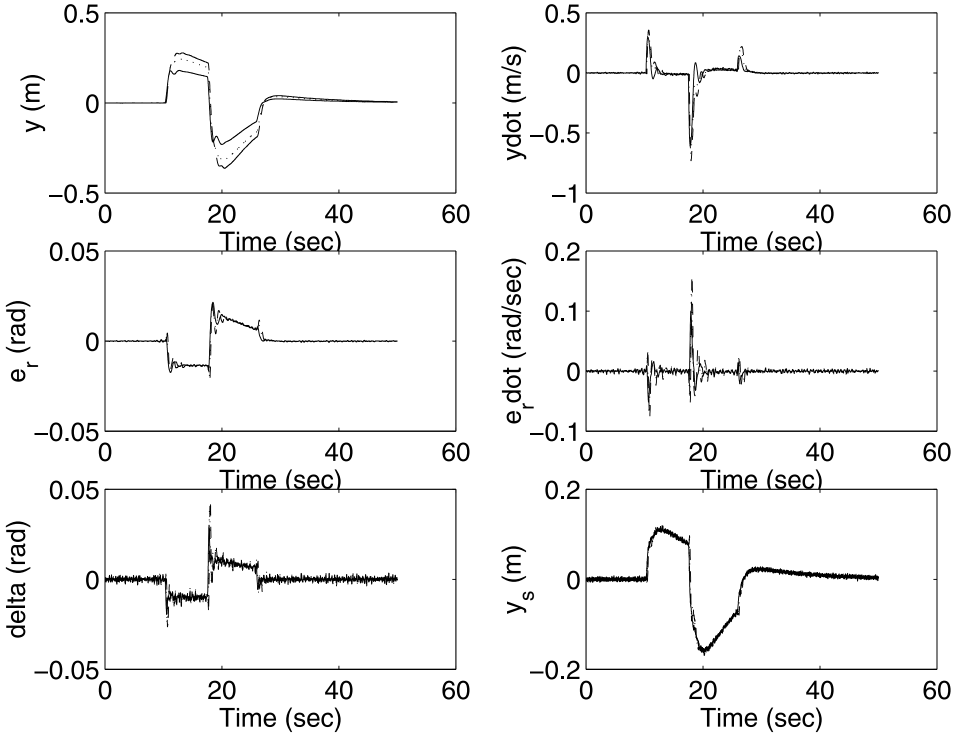

Figure 19: Simulation results for integrated lateral control with ALC and rear sensors (solid: first vehicle; dotted: second vehicle; dashed: third vehicle)

the information from the rear magnetometers alone, the lateral errors are larger, but the system responses are much smoother.

4.5 Summary

In this section, the IRIS sensor and autonomous lateral control were introduced. Control schemes for autonomous lateral control and integrated control that combines IRIS and rear magnetometers have been developed and tested by simulation. The simulation results show that the lateral errors of the following vehicles under ALC in a platoon increase in the upstream direction. When ALC is combined with the information from the rear magnetometers, these effects can be significantly reduced. The results show the the integrated control scheme is useful in improving tracking accuracy and smoothness of the vehicle lateral control system subject to magnetometer failures.

5 Conclusions

The performance of an existing vehicle lateral control system under several magnetometer fault scenarios was evaluated in simulations with both the bicycle model and the complex nonlinear model. Simulation results show that when front magnetometers fail the lateral control system is still stable although its performance deteriorates. But the lateral control system becomes unstable when rear magnetometers fail. This motivated the design of new lateral controllers, that stabilize the system and optimize the performance under faulty operation of magnetometers.

Since vehicle lateral dynamics is observable from the output of either the front or the rear set of magnetometers, output feedback controllers can be designed to stabilize the closed loop system with the output of either set of magnetometers. Two output feedback controllers were designed based on H_∞ optimal control theory, one using the output of front magnetometers and the other using the output of rear magnetometers. The synthesized controllers were optimal in the sense of minimizing the effects of the disturbance (road curvature) and sensor noise on the lateral error and control effort. Simulations were performed with these two controllers, and the performance was shown to be satisfactory at longitudinal velocities up to $30m/s$.

Autonomous lateral control was studied to deal with the situation when both the front and the rear sets of magnetometers fail. The lateral deviation and yaw angle of the controlled vehicle with respect to its preceding vehicle are obtained from IRIS. The autonomous lateral control algorithm allows the vehicle to follow a real-time trajectory of the preceding vehicle, which is calculated from the output of IRIS. Simulations were conducted with a platoon of three vehicles. The results show that autonomous lateral control causes accumulation of lateral errors in the upstream direction of the vehicle string. An integrated lateral control scheme that combines the information from IRIS and rear magnetometers was developed. Simulation results show that this integrated control scheme provides better tracking accuracy of the following vehicles than autonomous lateral control. The integrated control scheme also achieves smoother performance if compared to the results of lateral control that uses the information from rear magnetometers alone.

Acknowledgement

This project is sponsored by California PATH (Partners of Advanced Transit and Highways) program. The contents of this report reflect the views of the authors who are responsible for the facts and the accuracy of the data presented herein. The contents do not necessarily reflect the official views or policies of the state of California. This report does not constitute a standard, specification, or regulation. We also acknowledge the technical contributions of Dr. H-S. Tan, D. Nelson, and other researchers at Richmond Field Station.

References

[1] Fenton, R. E., Melocik, G. C. and Olson, K. W. (1976). "On the Steering of Automated Vehicles: Theory and Experiment", *IEEE Trans. on Automatic Control,* Vol AC-21, No. 3, June 1976, pp. 306-315

[2] Hingwe, P. and Tomizuka, M. (1997), "Experimental Evaluation of a Chatter Free Sliding Mode Controller for Lateral Control in AHS", *Proceedings of the 1997 American Control Conference,* Albuquerque, NM, 1997, pp. 3365-3369

[3] Lugner, P. (1997), "The Influence of the Structure of Automobile Models and Tyre Characteristics on the Theoretical Results of Steady-State and Transient Vehicle Performance", *The Dynamics of Vehicles, Proceedings of the 5th VSD-wnd IUAM Symposium,* Viena, Sustria, 1997

[4] Chen, C. and Tan, H-S. (1998). "Sterring Control of High Speed Vehicle: Dynamic Look Ahead and Yaw Rate Feedback", *Proceedings of the 37th IEEE, Conference on Decision Control,* Tampa, Florida USA, December 1998.

[5] Guldner, J., Tan, H-S. and Patwardhan, S. (1997). "Study of Design Directions for Lateral Vehicle Control", *Proceedings of the 36th Conference on Decision Control,* San Diego, California USA, December 1997.

[6] Patwardhan, S., Tan, H-S. and Guldner, J. (1997). "A general Framework for Automatic Steering Control: System Analysis", *Proceedings of the American Control Conference,* Albuquerque, New Mexico, June 1997.

[7] Peng, H. and Tomizuka, M. (1990), "Lateral Control of Front-Wheel Steering Rubber-Tire Vehicles", *California PATH Report,* UCB-ITS-PRR-90-5, July 1990

[8] Segel, L. (1956), "Theoretical Prediction and Experimental Substantiation of the Response of the Automobile to Steering Control", *Automobile Division, The Institute of Mechanical Engineers,* pp. 26-46

[9] Shladover, S. E, Wormley, D. N., Richardson, H. H. and Fish, R. (1978), "Steering Controller Design for Automated Guideway Transit Vehicles", *ASME Journal of Dynamic Systems, Measurement and Control,* Vol 100, March 1978, pp. 1-8

[10] Tan, H-S, Guldner, J., Patwardhan, S., Chen, C. and Bougler, B. (1999). "Development of an Automated Steering Vehicle Based Roadway Magnets - A Case Study of Mechatronic System Design", *IEEE/ASME Transitions on Mechatronics,* Vol 4, pp. 258-272